Foam-like Ce–Fe–O-based nanocomposites as catalytic platforms for efficient hydrogen oxidation in air

Journal of Science: Advanced Materials and Devices 8 (2023) 100596

Contents lists available at ScienceDirect

Journal of Science: Advanced Materials and Devices

journal homepage: www.elsevier.com/locate/jsamd

Original Article

Foam-like Ce–Fe–O-based nanocomposites as catalytic platforms for efficient hydrogen oxidation in air

Thanh Son Cam [a, b, *], Shamil Omarov [c], Andrey Trofimuk [c], Vasily Lebedev [d], Vitaly Panchuk [e], Valentin Semenov [e], Anh Tien Nguyen [f], Vadim Popkov [c]

[a] Institute of Fundamental and Applied Sciences, Duy Tan University, Ho Chi Minh City 700000, Vietnam
[b] Faculty of Environmental and Chemical Engineering, Duy Tan University, Da Nang 550000, Vietnam
[c] Ioffe Institute, Saint Petersburg 194021, Russia
[d] Bernal Institute, University of Limerick, Limerick V94 T9PX, Ireland
[e] Institute of Chemistry, Saint Petersburg State University, Saint-Petersburg 198504, Russia
[f] Faculty of Chemistry, Ho Chi Minh City University of Education, Ho Chi Minh City 700000, Vietnam

ARTICLE INFO

Article history:
Received 18 February 2023
Received in revised form
5 June 2023
Accepted 16 June 2023
Available online 13 July 2023

Keywords:
Hydrogen catalytic oxidation
Cerium orthoferrite
Perovskite
CeO_2–Fe_2O_3
Solution combustion synthesis
Glycine-nitrate condition

ABSTRACT

Foam-like nanocomposites of the Ce–Fe–O system with two (c-CeO_2, am-F_2O_3), three (c-CeO_2, o-$CeFeO_3$, α-F_2O_3), or four phases (c-CeO_2, o-$CeFeO_3$, α-F_2O_3, am-Fe_2O_3) were synthesized using the RedOx reaction of glycine-nitrate combustion. The glycine/nitrate ratio (*G/N*) varied from deficient (0.2, 0.4) and stoichiometric (0.6) to excess ratios of glycine (0.8, 1.0, 1.2, 1.4). PXRD, ^{57}Fe Mössbauer spectroscopy, N_2-physisorption, TEM, H_2-TPD, O_2-TPD, and H_2-TPR were used to examine the characteristics of the obtained samples. The average crystallite size of the obtained composites was in the range of 1.3–31.3 nm, 33.4–50.7 nm, and 10.1–33.9 nm for c-CeO_2, o-$CeFeO_3$, and α-Fe_2O_3, respectively. The lowest S_{BET} (1.5 m^2/g) belonged to the case of stoichiometric *G/N*, while the highest value (49.2 m^2/g) was found in the case of the highest amount of glycine (*G/N* = 1.4); the latter case also had the largest total pore volume ($V_p = 0.182$ cm^3/g) when compared to the others. Moreover, the advanced catalytic performance of foamy Ce–Fe–O-based nanocomposites toward H_2 combustion in air was found with $t_{10} = 275$ °C, $t_{50} = 345$ °C, and $E_a = 76.9$ kJ/mol for sample *G/N* = 1.2. The higher activity of sample *G/N* = 1.2 in catalysis was attributed to different properties of the composite, including an appropriate component phase ratio, the smaller size of crystallites, higher specific surface area, higher reducibility,oxygen capacity, etc. The findings make it possible to carry out the directed synthesis of catalysts based on the Ce–Fe–O system with specific phases, dispersion, and morphological composition for efficient hydrogen oxidation at moderate temperatures.

1. Introduction

Hydrogen can enter an airflow from various sources, such as hydrogen production equipment operations, hydrogen storage warehouses, fuel element zones, battery charging, and hydrogen refueling stations [1–3]. To avoid hydrogen explosions or fires in an enclosed air space, it is crucial to keep hydrogen concentrations below the explosion limits (18.3–59.0% in air) [4]. There are numerous aspects to consider when designing procedures and systems to prevent hydrogen-related accidents. One of these is the catalytic method for hydrogen removal (i.e., oxidizing hydrogen to form water) because of its dependability and simplicity in the presence of surrounding oxygen.

When oxygen and hydrogen come into contact with the prepared catalysts, the wanted reaction begins with an exothermic process, as shown in Reaction 1 [1].

$$2H_2 + O_2 \rightarrow 2H_2O + 244.9 \text{ kJ/mol} \quad \text{(R. 1)}$$

At high temperatures ($t > 500$ °C), in the absence of catalysts, the oxidation of hydrogen to steam occurs normally in the presence of oxygen. Catalysts are usually required during oxidation at lower

* Corresponding author. Institute of Fundamental and Applied Sciences (Ho Chi Minh City 700000), Faculty of Environmental and Chemical Engineering (Da Nang 550000), Duy Tan University, Vietnam.
E-mail addresses: camthanhson@duytan.edu.vn, camthanhson1108@gmail.com (T.S. Cam).

Peer review under responsibility of Vietnam National University, Hanoi.

https://doi.org/10.1016/j.jsamd.2023.100596

temperatures and/or in humid air. As is well known, metals from the Pt-group are most often used among the diverse range of catalysts for the oxidation of hydrogen [1,2,5]. However, due to the scarcity of noble metals, high price, and sensitivity to sulfur poisoning, experts are focusing their efforts on developing new catalysts based on inexpensive metal oxides that have relatively high catalytic operability and durability and especially perform at low temperatures when dealing with hydrogen reactions.

A European patent application in 2014 [6] given by T.C. Golden et al. pointed out a simple mechanism for carbon monoxide and hydrogen removal using a copper/manganese-based catalyst (hopcalite) as follows:

$$\text{CO or } H_2 \text{ (gas)} \rightleftarrows \text{CO or } H_2 \text{ (adsorbed)}$$

$$\text{CO or } H_2 \text{ (adsorbed)} + \text{O (surface)} \rightleftarrows CO_2 \text{ or } H_2O \text{ (adsorbed)}$$

$$CO_2 \text{ or } H_2O \text{ (adsorbed)} \rightleftarrows CO_2 \text{ or } H_2O \text{ (}\mathit{gas}\text{)}$$

But hopcalite is very effective in converting CO to CO_2, and H_2 oxidation frequently occurs after CO and CO_2 removal. As a result, new approaches for eliminating H_2 in the first step are required.

Recently, a work reported by A.N. Matveyeva et al. [7] expressed that the $CeFeO_3$-based catalyst exhibits a high activity toward CO_2 hydrogenation, which is explained by the fact that both perovskite $CeFeO_3$ and CeO_2 compounds can generate more oxygen vacancies and encourage oxygen ion migration, while the Fe_2O_3 particles aid in the movement of the oxygen lattice from the subsurface to the surface. Partially producing Ce^{3+} species on the CeO_2 lattice due to Frenkel-type anion defects as a result of oxygen vacancy generation is determined by our previous works [8,9].

Rare earth perovskites and Ce–Fe–O-based nanocomposites are commonly applied as catalysts for different chemical reactions like CO hydrogenation [10], ethylbenzene oxidation [11], CO and CH_4 transformation [12]. Cerium orthoferrite ($CeFeO_3$), in particular, can also be effective in the photocatalytic oxidation of methylene blue [13], organic pollutant degradation, nitrogen fixation [14], and other applications. To obtain the $CeFeO_3$ compound, various synthetic methods are used, such as the microwave process [15,16], co-precipitation with specific heating cycles [17], solid–state reactions [18,19], directly from CeO_2/Fe_2O_3/Fe components [20], or solution combustion synthesis [7,21–24].

The latter approach has emerged as one of the most promising methods because of its effortless, inexpensive, and targeted synthesis of nanostructured oxide materials. The relatively high temperature in the reaction zone, which can sometimes exceed 1200 °C for a short time, allows for the formation of nanosized oxide particles with amorphous and/or crystalline structures. Simultaneously, the process's high speed is accompanied by an abundant release of gaseous substances, which prevent sintering and recrystallization and thus provide a high dispersion of the products [21].

The properties of $CeO_2/Fe_2O_3/CeFeO_3$-based materials mentioned above are expected to facilitate hydrogen chemisorption, provide surface oxygen, and thus produce steam, i.e., remove hydrogen. Therefore, the current work aims to study the best condition (RedOx ratio) of a simple method (glycine-nitrate combustion) for synthesizing the catalysts based on the Ce–Fe–O system, investigating their physicochemical characteristics as well as testing their oxidizing properties concerning hydrogen oxidation.

2. Experimental

2.1. Catalyst preparation

0.5 g of catalysts were synthesized by the solution combustion method (SCS) using the following RedOx reaction (R. 2), as previously reported [23–26]. Cerium(III) nitrate hexahydrate ($Ce(NO_3)_3 \cdot 6H_2O$, 99%), iron(III) nitrate nonahydrate ($Fe(NO_3)_3 \cdot 9H_2O$, 98%), and glycine ($C_2H_5NO_2$, 98%) were used as reagents. These substances were purchased and used without being purified further.

$$3Ce(NO_3)_3 + 3Fe(NO_3)_3 + 10C_2H_5NO_2 = 3CeFeO_3 + 25H_2O\uparrow + 14N_2\uparrow + 20CO_2\uparrow \quad \text{(R. 2)}$$

The glycine/nitrate ratio (*G/N*) was calculated by the formula below (Eq. (1)). The *G/N* of the reaction's stoichiometric case was about 0.6; other samples with different *G/N* values of deficient (0.2, 0.4) and excess glycine (0.8, 1.0, 1.2, 1.4) were also obtained.

$$G/N = \frac{n(C_2H_5NO_2)}{\sum n\ (NO_3^-)} \quad \text{(Eq. 1)}$$

where $n\ (C_2H_5NO_2)$ – number of moles of glycine; $\Sigma n(NO_3^-)$ – total number of moles of nitrate groups.

The synthesis procedure was carried out as follows: first, glycine was dissolved in a minimum amount of distilled water; then, metal nitrates were added to the mixture; and finally, the solution was stirred until all components were completely dissolved. The resulting solution was then poured into a glassy carbon glass, which was heated in air on an electric hot plate (stove) until the water in the solution was completely evaporated, causing the reaction mixture to foam, ignite, and burn, resulting in the formation of a friable powder. The synthesized products were ground with a mortar and pestle before being analyzed for their properties.

2.2. Catalyst characterization

An X-ray diffractometer (RIGAKU SmartLab 3) with monochromatic CuK_α radiation of 0.15406 nm and a Bragg angle of 20–65° was used to determine the phase composition. To acquire the mole fraction of the identified phases, an internal standard was introduced into the studied samples, for which the cubic modification of silicon was used. The resulting data were processed with the help of the Rietveld and Origin applications. The Scherrer equation (Eq. 2) was applied to calculate the average crystallite size (D) of CeO_2, Fe_2O_3, and $CeFeO_3$ crystallites using Miller indices (hkl) of the XRD peak at maximum intensity.

$$D = \frac{0.94 \cdot \lambda}{\beta \cdot \cos(\theta)}, \quad \text{(Eq. 2)}$$

where 0.94 is the Scherrer constant for spherical nanoparticles; λ is the X-ray wavelength, nm; β is the full width at half maximum of peaks, radian; θ is the Bragg angle, radian.

^{57}Fe Mössbauer spectroscopy was studied on a Wissel GmbH multifunctional Mössbauer spectrometer. The obtained spectra were decomposed into components based on the Lorentz spectral distribution of moments using the Levenberg–Marquardt algorithm.

Brunauer–Emmett–Teller specific surface area (S_{BET}) of nanopowders was determined from nitrogen adsorption isotherms at 77 K (−196 °C) and measured with a Micrometrics ASAP-2020. Equation (3) was handled to evaluate the total pore volume (V_p) of the obtained materials.

$$V_p = \frac{Q_{0.99}}{647}, \tag{Eq. 3}$$

where V_p is the single point adsorption total specific pore volume of pores at the relative pressure $P/P_0 \approx 0.99$ (cm^3/g STP); $Q_{0.99}$ is the highest quantity adsorbed in volume at the P/P_0 of 0.99 (cm^3/g STP); 647 is the gas/liquid ratio constant for liquid nitrogen [27].

A JEOL-TEM-100CX transmission electron microscope was employed to observe the morphology and spatial distribution of the sample phases.

Temperature-programmed desorption of hydrogen (H_2-TPD) and oxygen (O_2-TPD) were performed on Chemosorb (SOLO, Novosibirsk, Russia) with a thermal conductivity detector (TCD). About 120–150 mg of a sample was first preheated in situ under Ar or O_2/He (50:50 vol%) flow (20 or 40 mL/min, respectively) at a ramp rate of 20 °C/min to 500 or 600 °C for 30 min (a sample of *G/N* = 0.8 was preheated in a He flow at 600 °C for 30 min), for the H_2-TPD or O_2-TPD tests, respectively. Then it was cooled to 50 or 30 °C in the same gas flow and saturated with H_2 or O_2 for 20 min, respectively. The sample was then heated to 500 or 800 °C at a ramping rate of 10 °C/min after removing the physically adsorbed H_2 or O_2 by purging with Ar or He (20 mL/min), respectively. To calculate the surface density ($\rho(H_2)$ and $\rho(O_2)$, nm^{-2}) of desorbed hydrogen and oxygen in the temperature range of 50–400 and 25–600 °C, respectively, the following equation was used:

$$\rho = \frac{n \cdot N_A \cdot 10^{-6}}{S_{BET} \cdot 10^{18}}, \tag{Eq. 4}$$

where n – amount of desorbed H_2 or O_2, μmol/g; N_A – Avogadro constant, $6.023 \cdot 10^{23}$ mol^{-1}.

In H_2-TPR tests, about 40 mg of a sample pretreated at 500 °C in air for 30 min (a sample of *G/N* = 0.8 was not pretreated in order to avoid destruction of the $CeFeO_3$ phase) was reduced from 50 to 700 °C at a ramp rate of 10 °C/min under 10 vol% H_2 in Ar (20 mL/min). Isopropanol, cooled in liquid nitrogen, was used as a water trap. CuO was applied to calibrate hydrogen consumption.

2.3. Catalytic test

Catalytic hydrogen combustion was performed with a feed mixture of 2.5 vol% of H_2 in air at a total flow rate of 100 cm^3/min and a gas hourly space velocity (GHSV) of 30 000 h^{-1}. A hydrogen generator was used to produce dried, 99.999% pure hydrogen. A compressor with desiccant columns served as the dry air source. Gas flow regulators were used to obtain the desired composition of gas flow. Catalytic experiments were carried out in a packed-bed stainless steel reactor tube (35 cm in length and 0.8 cm in interior diameter) that was isothermally controlled at atmospheric pressure and temperatures ranging from 150 to 470 °C. The reactor was loaded with 200 mg of powdered catalyst. To dry the gas flow, a moisture trap containing $CaCl_2$ and silica gel granules in a Drexel bottle was placed at the reactor's outlet. A gas chromatograph equipped with a thermal conductivity detector (Ar used as a carrier gas, 30 mL/min) was applied to analyze the product gas streams. To separate the mixture of H_2, N_2, and O_2, a molecular sieve CaA column (length x inner diameter = 3 m × 3 mm, CaA fraction = 0.25–0.5 mm, thermostat temperature = 80 °C) was used.

In general, the rate of hydrogen oxidation is determined by the concentrations of H_2 and O_2, with the same or different orders for each. This is especially true at their close concentrations [28]. However, in the presence of an excess of oxygen, the rate of reaction is primarily determined by the concentration of hydrogen [29–31]. As a result, the equation for the observed reaction rate with respect to H_2 takes the following form:

$$r^{obs} = A^{obs} \cdot e^{\frac{-E_a^{obs}}{R \cdot T}} \cdot P(H_2) \tag{Eq. 5}$$

or in logarithmic form:

$$ln\left(r^{obs}\right) = -E_a^{obs} \cdot \frac{1}{RT} + \ln\left(A^{obs}\right) + \ln(P(H_2)), \tag{Eq. 6}$$

where $P(H_2)$ – current partial pressure of H_2 in the flow, atm ($P(H_2) = P_0(H_2) \cdot (1 - x(H_2)$, $P_0(H_2)$ – initial H_2 partial pressure, 0.025 atm); E_a^{obs} – observed activation energy, kJ/mol; A^{obs} –observed pre-exponential factor, mmol/(s·m^2·atm); R – universal gas constant, given $8.314 \cdot 10^{-3}$ kJ/(mol·K); T – temperature of H_2 conversion, K; r^{obs} – observed rate of H_2 oxidation reaction, mmol/(s·g), converted to mmol/(s·m^2) as related to S_{BET}, the following equation (Eq. 7) was used to determine the value r^{obs}.

$$r^{obs} = \frac{F_{in} \cdot [H_2]_0 \cdot x(H_2)}{m \cdot 22.4}, \tag{Eq. 7}$$

where F_{in} – initial volume flow rate, ml/s; 22.4 mL/mmol – molar gas volume at standard temperature and pressure; $[H_2]_0$ – concentration of H_2 in the inlet gas flow, mol%; $x(H_2)$ – percentage H_2 conversion at a specific temperature, %; m – catalyst weight, g.

3. Results and discussion

3.1. Phase composition and crystallite size

To analyze the phase and structural transformations of the obtained samples with various *G/N* ratios, the powder X-ray diffraction (PXRD) and ^{57}Fe Mössbauer spectroscopy (MS) were carried out. The use of these two analysis methods is due to the limitations of PXRD associated with the inability of studying the system's amorphous components, which, using MS, can be successfully characterized and quantitatively measured. When the results of these methods are compared (Fig. 1), it is clear that the samples with *G/N* values of 0.2 and 1.4 contain only two phases: cubic crystal structure CeO_2 (c-CeO_2; space group Fm-3m) and amorphous Fe_2O_3 (am-Fe_2O_3). The calculated molar fraction (Fig. 2a) from PXRD and MS analyses shows that the c-CeO_2 phase exists in the crystalline form for all samples with a little change in mole quantity, while the phase of am-Fe_2O_3 gradually transforms into mixtures of rhombohedral (α-Fe_2O_3; space group R-3cH) and cerium orthoferrite crystallites (o-$CeFeO_3$; space group Pbnm), where the *G/N* ratio varies from a glycine content that is deficient and excess to one that is stoichiometric (*G/N* = 0.6). It is worth noting that the highest molar fraction of the o-$CeFeO_3$ phase is found in the *G/N* ranges of 0.4–0.8.

The calculated average crystallite size (D) of nanoparticles is depicted in Fig. 2b. Without taking into account the samples with *G/N* values of 0.2 and 1.4, where only tiny crystalline particles of c-CeO_2 with $D \approx 1.5$ nm can be examined (in these cases, the growth of D(c-CeO_2) is most likely hampered by the large am-Fe_2O_3 particles), the D of c-CeO_2, o-$CeFeO_3$, and α-Fe_2O_3 decreases with increasing *G/N* ratios (0.4–1.2) from 31.3 to 2.2 nm, 50.7–33.4 nm, and 33.9–10.1 nm, respectively. A significant decrease in the average size of crystallites and the phase transformations can be

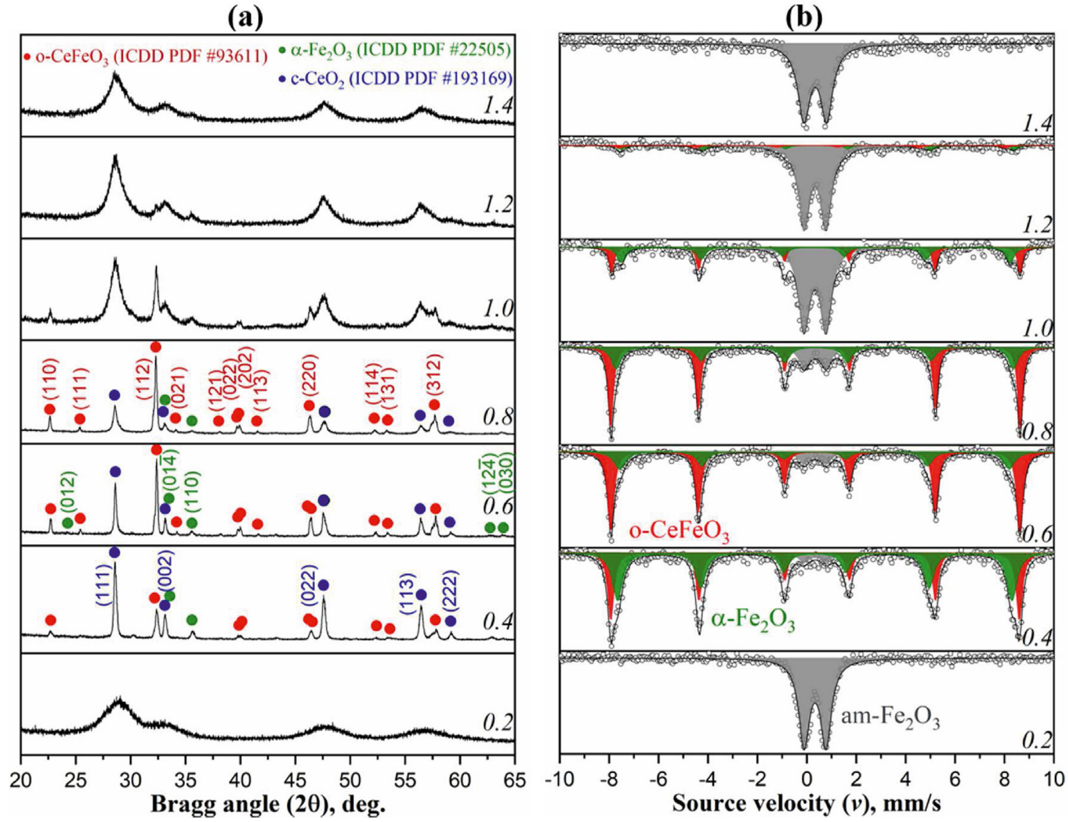

Fig. 1. PXRD patterns (**a**) and ^{57}Fe Mössbauer spectra (**b**) of the synthesized nanopowders.

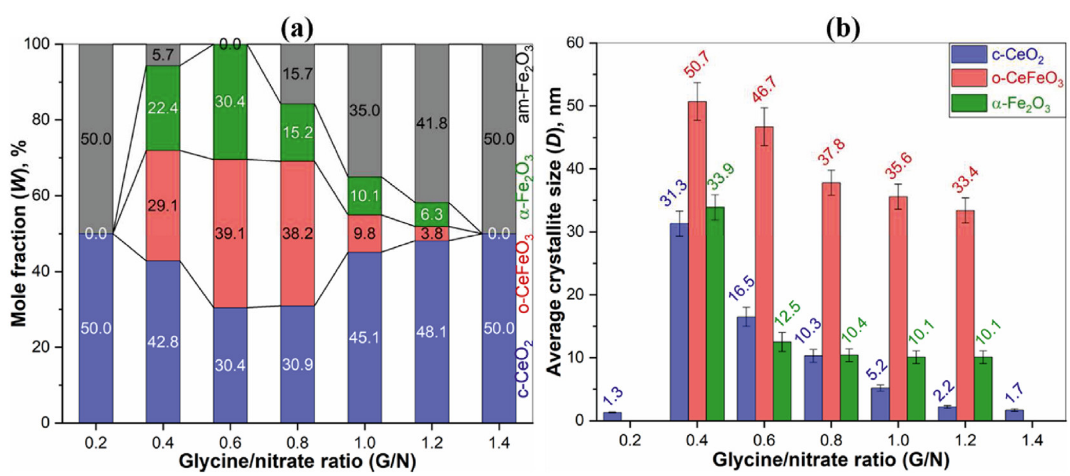

Fig. 2. Phase composition (**a**) and average crystallite size (**b**) of the obtained nanoparticles.

explained by the combustion mode of the synthesis process, which changes depending on the *G/N* ratios; for this, the temperature in the combustion reaction zone is the main explainable factor. In particular, the temperature in the reaction zone of the volume combustion mode (*G/N* = 0.4−0.8) is typically higher than that of the smoldering (*G/N* = 0.2) and self-propagating combustion (*G/N* = 1.0−1.4), which promotes active recrystallization and, as a result, an increase in the size of crystallites as well as a variation in phase quantity-quality [21,32].

3.2. Adsorption-structural and morphological features

The results of the N_2 physisorption analysis are shown in Fig. 3. The drawing curves in Fig. 3a show a type IVa isotherm for samples obtained from smoldering and self-propagating combustion, which is typical for mesoporous adsorbents according to the IUPAC classification of physisorption isotherms [7,33]. This statement is supported by the results of density functional theory (DFT): pore size distribution with maximum pore widths of 40 and 50 nm (see inset in Fig. 3a). Furthermore, the isotherms are accompanied by an H4-type hysteresis loop [33], which is frequently observed by aggregated crystallites. On the other hand, for samples obtained from volume combustion, a type of II isotherm is depicted, which is provided by nonporous or macroporous materials; the pore size distribution results also confirm this fact.

The specific surface area (S_{BET}) and total pore volume (V_p) of nanocrystalline materials are important characteristics that determine their functional properties in many cases. The S_{BET} value of the synthesized samples obtained in this work (Fig. 3b) correlates with crystallite size and form of phase composition, and thus with *G/N* ratios. Particularly, samples with the *G/N* ratio near the stoichiometric range (0.4–0.8) have the lowest S_{BET} (1.8–5.8 m^2/g) due to a high degree of crystalline formation with larger *D* and nonporous particles. In addition, the presence of more am-Fe_2O_3 phase in the nanopowders, combined with a smaller *D* of the crystalline phases, practically raises the value of S_{BET}. The higher S_{BET} of 49.2 m^2/g ($G/N = 1.4$) compared to S_{BET} of 32.7 m^2/g ($G/N = 0.2$) can be attributed to a higher amount of gases due to incomplete combustion, which leads to the formation of intermediate forms of combustion products (CO_x, NO_x), resulting in a more porous surface of the materials [21,34]. As shown in Fig. 3b, the total pore volume correlates with conditions of glycine-nitrate combustion and has a change tendency similar to S_{BET}. Like S_{BET}, the maximum value of V_p (0.182 cm^3/g) also belongs to the case of $G/N = 1.4$.

To study the formation of morphological features of compositions based on nanostructured particles c-CeO_2, am-Fe_2O_3, α-Fe_2O_3, and o-$CeFeO_3$ under conditions of glycine-nitrate combustion, three samples (G/N = 0.2, 0.6, 1.4) representing three modes of combustion were investigated by transmission electron microscopy (TEM). The resulting images show micro-sized agglomerates with a foamy morphology (Fig. 4a,c,e). The formation of nanostructured compositions in the cases with *G/N* values of 0.2 and 1.4 is quite similar to each other and consists of very small crystallites of c-CeO_2 surrounded by am-Fe_2O_3 particles. The obtained selected area electron diffractions (SAED) in Fig. 4b,f show intensive diffraction circles with interplanar distances of main reflexes referring to those of the c-CeO_2 crystallites; no other notable diffraction circles were observed, confirming Fe_2O_3 particles presence in the amorphous form. Notice that the sample with a high degree of crystallinity is formed at $G/N = 0.6$ (Fig. 4c), which is displayed by a spot diffraction pattern (white dots on a black background) (Fig. 4d). These SAED and TEM results match those obtained from PXRD data. It is obvious that changing the *G/N* ratio affects the microstructure of the resulting phases as well as the dispersed composition of the obtained nanopowders [9].

Based on the generalization of the obtained information on chemical, phase, and dispersed features of glycine-nitrate combustion products with different *G/N* ratios, a schematic illustration for changing phase composition depending on the *G/N* ratio is proposed (Fig. 5). According to the presented scheme, at $G/N = 0.2$, the finely dispersed Ce–O–Fe matrix grows to form nanocrystallites of CeO_2 and then remains crystalline throughout the other *G/N* ratios; only the crystallite size of CeO_2 is variable, as mentioned in Fig. 2b. At the same time, the modification of Fe_2O_3 exists in the amorphous form for almost all cases of synthesized *G/N*, except for the stoichiometric condition, where about all particles are crystallized, as confirmed by PXRD, MS, and TEM results. It is demonstrated that two phases of α-Fe_2O_3 and o-$CeFeO_3$ always appear together when the Fe_2O_3 crystallites are processed.

3.3. Reducibility, H_2 and O_2 desorption

An important characteristic of cerium and iron is their ability to have several oxidation states depending on the environment and external conditions. Therefore, it is necessary to study the interaction of the obtained composites with H_2 and O_2. Fig. 6 shows the curves of H_2 consumption during the temperature-programmed reduction (TPR) of samples G/N = 0.2, 0.8, and 1.4.

Comparison of the reduction profiles of G/N = 0.2 and 1.4 samples with literature data on the CeO_x-FeO_x system [7,35–38] shows that the peaks mainly correspond to the stepwise reduction of Fe_2O_3 to Fe^0 through Fe_3O_4 and FeO: Fe_2O_3 to Fe_3O_4 (412–424 °C), Fe_3O_4 to FeO (about 546–573 °C), and then to Fe (588–644 °C). The profiles also show an overlap of several peaks that were separated by Gaussian curves. Fe_2O_3 is generally characterized by one component up to 450 °C [35,36,38]. The peak at 395–399 °C revealed in this work is apparently associated with the reduction of Fe_2O_3 nanoparticles in good contact with CeO_2 [35]. This effect can be explained by the ability of CeO_2 to adsorb H_2 heterolytically [39], which facilitates the subsequent reaction of hydrogen with Fe_2O_3 surface oxygen. Nanosized CeO_2 is characterized by a wide-range peak at 400–600 °C with a maximum at 500–570 °C, corresponding to the reduction of surface and near-surface Ce^{4+} atoms to Ce^{3+} [40–42]. This peak is not recognizable against much stronger FeO_x reduction peaks or may be present as a "background" between the two main FeO_x reduction regions.

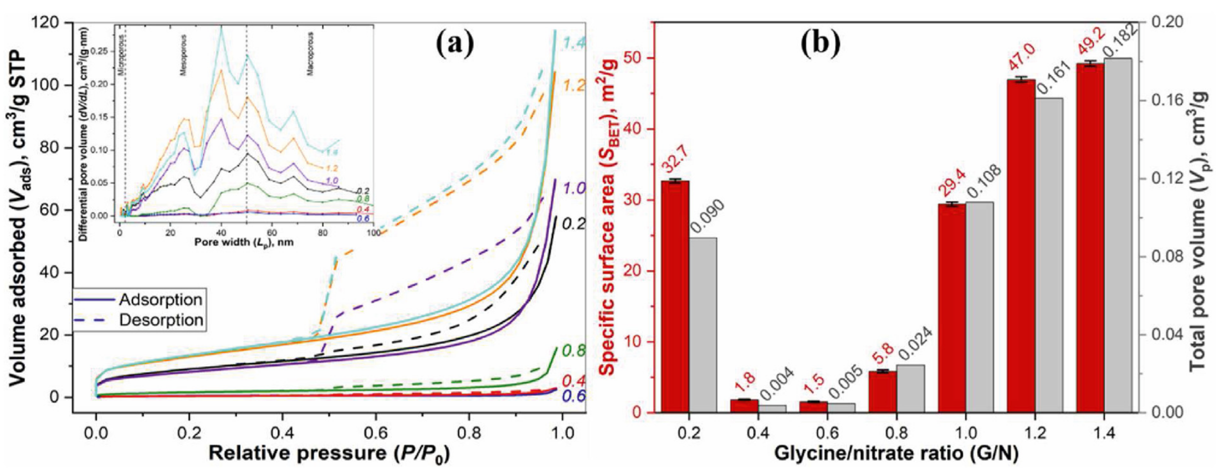

Fig. 3. Nitrogen physisorption isotherms and DFT pore size distribution (**a**); Specific surface area and total pore volume of the synthesized samples (**b**).

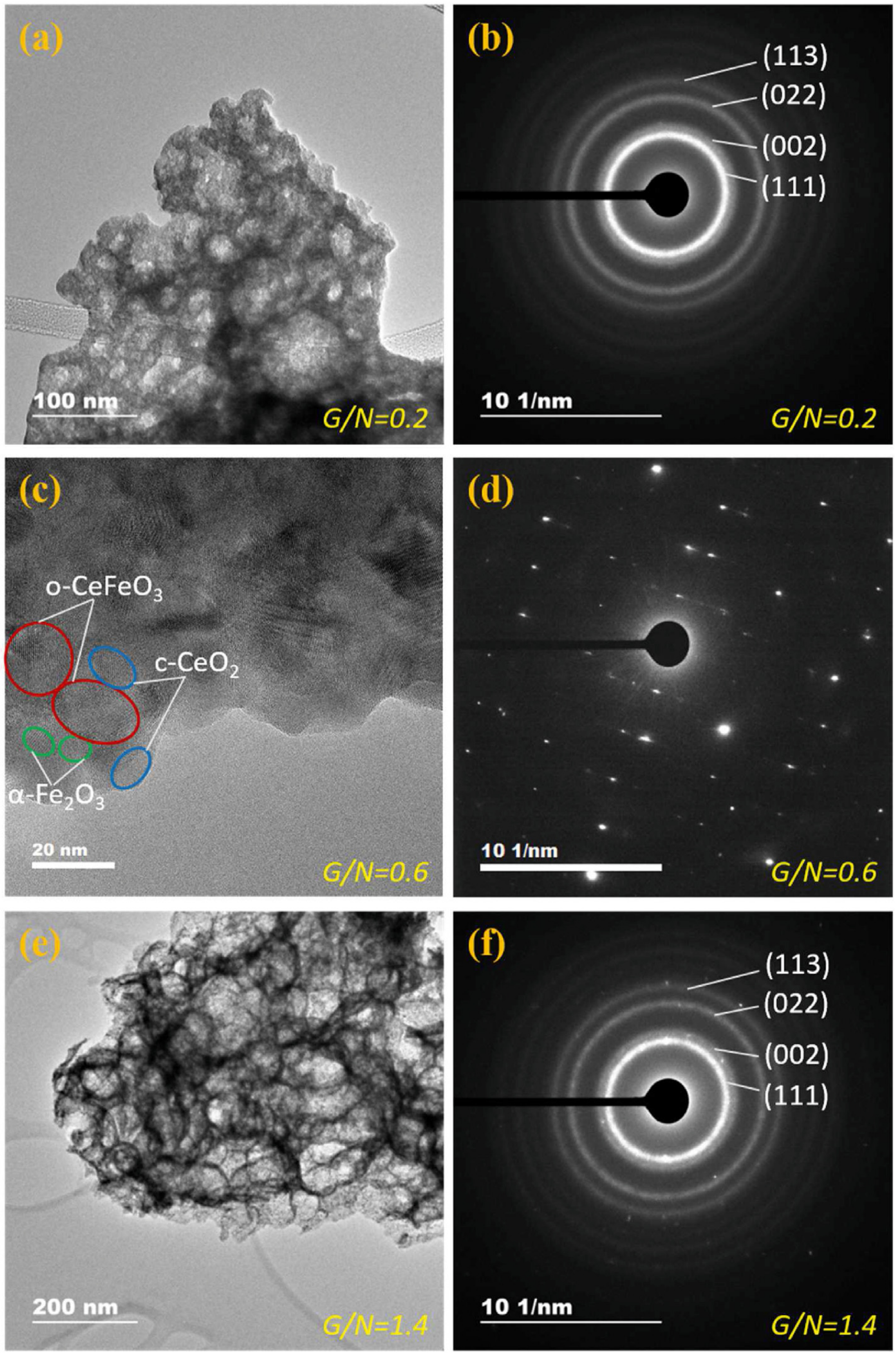

Fig. 4. TEM images (**a**, **c**, **e**) and SAED patterns (**b**, **d**, **f**) of the obtained nanocomposites with various *G/N* ratios.

The reducibility of the sample $G/N = 0.8$ is significantly lower compared to other studied samples. It is characterized by at least three hydrogen consumption peaks at 433, 492, and >600 °C. The last peak corresponds to the reduction of bulk Fe^{3+} during the decomposition of $CeFeO_3$ in a reducing medium as well as the reduction of bulk Ce^{4+} in free CeO_2 particles. Peaks in the region of 350−600 °C, apparently correspond to the partial reduction of Fe^{3+} in free Fe_2O_3 nanoparticles as well as surface Fe^{3+} ions in $CeFeO_3$ [7]. The latter leads to the formation of surface oxygen vacancies in $CeFeO_3$. The reduction of surface and subsurface Ce^{4+} in unbound CeO_2 cannot be completely ruled out. However, due to the small specific surface of the sample, the CeO_2 surface available for reduction is not high compared to the samples $G/N = 0.2$ and 1.4. $LaFeO_3$ is characterized by the reduction of Fe^{4+} to Fe^{3+} at 250−400 °C [43]. A similar peak for sample $G/N = 0.8$ was not observed.

Fig. 7 shows the temperature-programmed desorption (TPD) curves of H_2 and O_2 for samples $G/N = 0.2$, 0.8, and 1.4. Most of the hydrogen is desorbed up to 350 °C, typical for both CeO_2 and Fe_2O_3 [38,39,44,45]. Broad and overlapping H_2 desorption peaks indicate that hydrogen is adsorbed on surface oxygen ions in different environments and/or coordination. Some differences in the desorption profiles for samples $G/N = 0.2$ and 1.4 can be associated with a slight difference in the size of nanoparticles, their interaction with

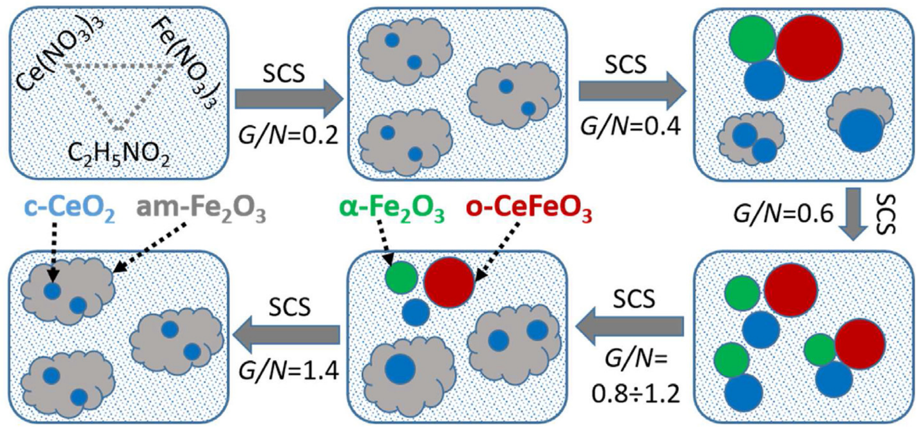

Fig. 5. Schematic illustration of the phase composition change of Ce–Fe–O-based nanocomposite obtained by glycine-nitrate combustion with different *G/N* ratios.

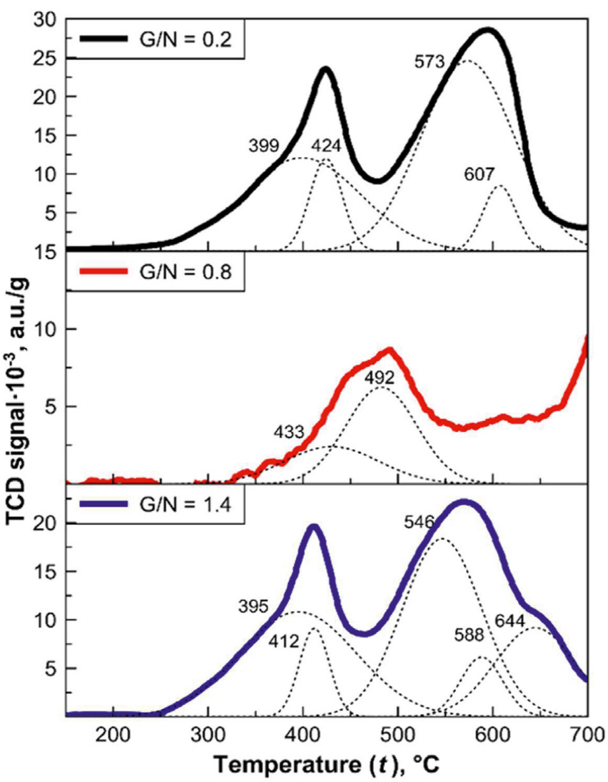

Fig. 6. H_2-TPR curves for the Ce–Fe–O system of samples $G/N = 0.2$, 0.8, and 1.4.

each other, and the accessibility of crystalline planes [39]. For the sample with the amount of $CeFeO_3$ phase close to the maximum ($G/N = 0.8$), H_2 desorption is also observed, which may be related to the adsorption on its surface cations since the size of CeO_2 and Fe_2O_3 crystallites in this sample is large in comparison with the samples $G/N = 0.2$ and 1.4. The quantitative comparison shows that $G/N = 0.8$ is characterized by a minimum amount of desorbed H_2 per gram of sample $n(H_2)$ but a maximum surface density of desorbing sites ($\rho(H_2)$) (Table 1).

A small amount of O_2 is desorbed for samples $G/N = 0.2$ and 1.4 up to 200 °C and more O_2 is desorbed after 200 °C. The peak at low temperatures apparently corresponds to the desorption of O_2 in the form O^{2-} or O_2^{2-} from oxygen vacancies, while the main peak corresponds to the desorption of atomic oxygen or partial crystalline oxygen evolved from the bulk of CeO_2 [46,47]. As noted in [47], there is a second form of oxygen that promotes soot oxidation due to migration from the surface lattice site to neighboring vacancies with subsequent removal from the catalyst surface. In contrast to the considered samples, for sample $G/N = 0.8$, a wide and low-intensity desorption peak up to 400 °C is observed, which apparently corresponds to the desorption of the first form of oxygen. A peak in the same temperature range was observed for $LaFeO_3$ [48]. Also, for sample $G/N = 0.8$, a low-intensity peak of the second form of oxygen is observed above 500 °C. The desorbed amount of O_2 per gram of sample ($n(O_2)$) and the surface density of desorbing sites ($\rho(O_2)$) have a trend similar to the results of H_2-TPD (Table 1).

3.4. Catalytic performance

The temperature dependence of the percentage H_2 conversion (x_{H_2}) is depicted in Fig. 8. As expected, catalysts with higher S_{BET} ($G/N = 0.2$, 1.2, 1.4) have higher activity; in this context, the temperatures of 10% (t_{10}) and 50% (t_{50}) H_2 conversion for case $G/N = 1.2$ are the lowest at about 275 °C and 345 °C, respectively. It should be noted that the sample with $G/N = 1.2$ differs from those with $G/N = 0.2$ and 1.4 by containing a small amount of the crystalline forms o-$CeFeO_3$ and α-Fe_2O_3 rather than only two phases c-CeO_2 and am-Fe_2O_3 in the other cases. So, it may conclude that a nanocomposite based on a certain phase ratio of c-CeO_2/o-$CeFeO_3$/α-Fe_2O_3/am-Fe_2O_3 ispreferred in hydrogen catalytic oxidation. Further, it can be seen that samples with near-stoichiometric G/N values ($G/N = 0.4$, 0.6, 0.8) perform poorly in catalytic activity when the x_{H_2} does not reach 30% at around 500 °C, which can be explained on the one hand by their low S_{BET} and, on the other hand, by a high amount of o-$CeFeO_3$ and α-Fe_2O_3 phases as well as a large crystallite size. On the curves of samples with the highest content of $CeFeO_3$ ($G/N = 0.6$ and 0.8), one can note an increased H_2 conversion at temperatures of 300–450 °C compared to the sample with $G/N = 0.4$; this is associated with the achievement of the temperature at the beginning of the decomposition of $CeFeO_3$ to CeO_2 and Fe_2O_3 [7,23].

Based on the results in Fig. 8a, the slope of the linear portion of the curve was used to calculate the reaction rates (see Eqs. (5)–(7) in Section 2.3) over these catalysts at various temperatures [49,50]. Samples $G/N = 0.2$, 1.2, and 1.4 have higher catalytic activity but higher E_a^{obs} (observed activation energy) (Fig. 9). They are characterized by a lower temperature at the beginning of the reduction of Fe_2O_3 with different localization to Fe_3O_4 (appearance of Fe^{2+}) and surface Ce^{4+} to Ce^{3+}, coinciding with the temperature range of the beginning of active hydrogen oxidation (200–300 °C). The

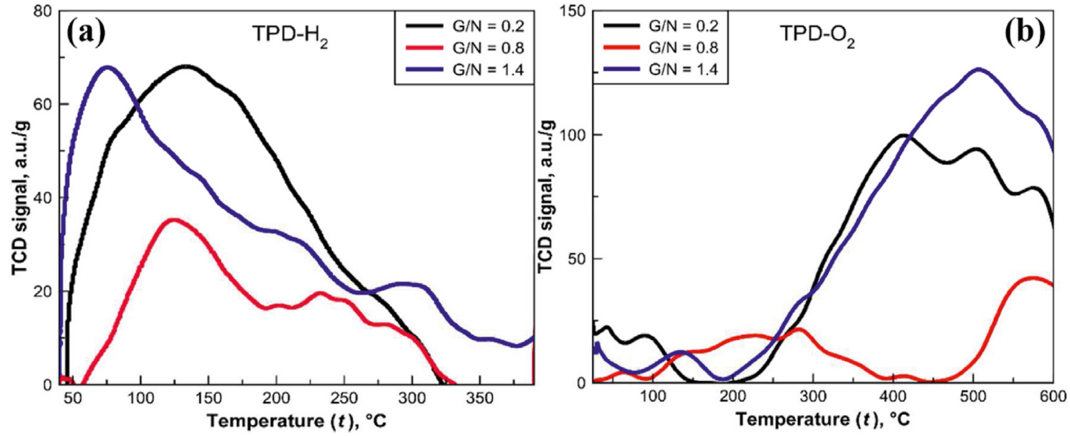

Fig. 7. H_2-TPD (**a**) and O_2-TPD (**b**) curves for the Ce–Fe–O system of samples *G/N* = 0.2, 0.8, and 1.4.

Table 1
Calculation results from H_2-TPD and O_2-TPD curves.

G/N	$n(H_2)$, μmol/g	$\rho(H_2)$, nm^{-2}	$n(O_2)$, μmol/g	$\rho(O_2)$, nm^{-2}
0.2	14.4	0.3	111.2	2.0
0.8	6.2	0.7	28.0	2.9
1.4	9.4	0.1	124.3	1.5

desorption of atomic oxygen from bulk CeO_2 also begins in this temperature range. A similar effect of reducibility and oxygen capacity on the example of Fe_2O_3 catalysts for the oxidation of CO and CeO_2 or $Ce_{0.9}Ni_{0.1}O_{2-\delta}$ catalysts for the oxidation of soot or hydrogen was observed in [41,42,50,51].

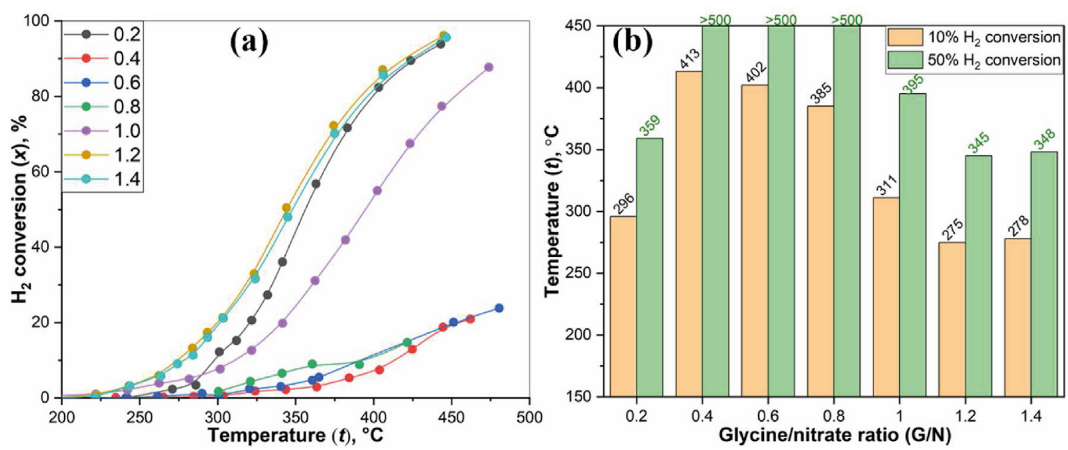

Fig. 8. Temperature dependence of percentage H_2 conversion (**a**); the temperature for 10% and 50% H_2 conversion (**b**).

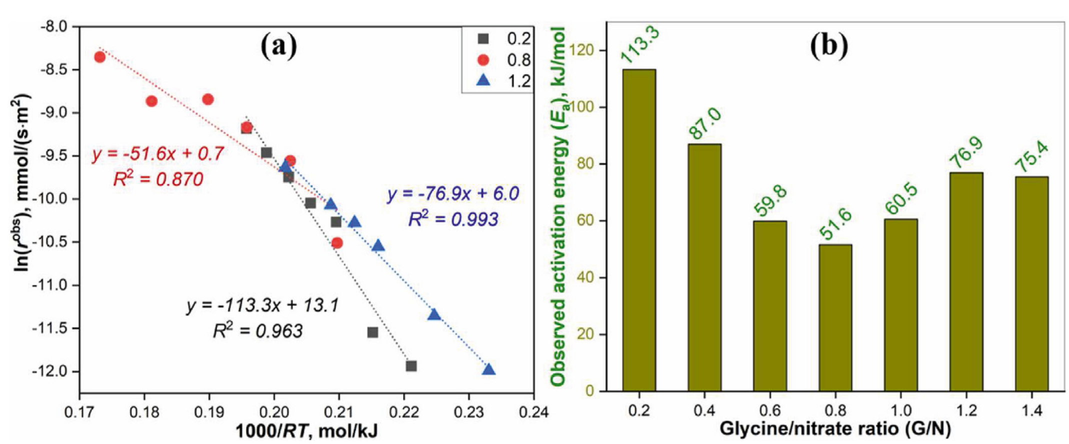

Fig. 9. The observed rate constant of the H_2 oxidation reaction as a function of temperature (**a**); the *G/N* dependence of the observed activation energy (**b**).

Table 2
Observed activation energy of hydrogen oxidation for different catalytic systems.

Sample	E_a^{obs}, kJ/mol	Reaction conditions	Ref.
$Ce_{0.95}Cu_{0.05}O_{2-\delta}$	15	Fixed-bed reactor, 2.7 vol% H_2 + 2.7 vol% O_2 + balance N_2, GHSV = 42 310 h^{-1}	[49]
$Ce_{0.9}Ni_{0.1}O_{2-\delta}$	48	Fixed-bed reactor, 2.7 vol% H_2 + 2.7 vol% O_2 + balance N_2, GHSV = 48 000 h^{-1}	[50]
CeO_2 cubes	70 ± 20	H_2-TPR, 60 mL/min, 5% H_2/Ar	[42]
CeO_2 rods	130 ± 20		
CeO_2 octahedrons	150 ± 20		
$LaMn_{0.8}B_{0.2}O_3$ (B=Ni, Zn, Cu)	53–67	Recirculation fixed-bed reactor (40:1), 0.2–2 vol% H_2 in air	[54]
G/N = 0.2	113	Fixed-bed reactor, 2.5 vol% H_2 in air, GHSV = 30 000 h^{-1}	This work
G/N = 0.8	52		
G/N = 1.4	75		

The sample *G/N* = 0.8 has much lower activity, which can additionally be explained by the lower reducibility and oxygen capacity. However, it has a higher density of O_2 and H_2 desorption sites as well as a lower observed activation energy. Bao et al. [52] showed that the rate of CO oxidation over Fe_2O_3–CeO_2 increased with an increase in the density of surface oxygen vacancies. In [42], it was demonstrated that the activation energy of hydrogen oxidation over CeO_2 depends on the shape of the CeO_2 particles: 70 kJ/mol for nanocubes, 130 kJ/mol for nanorods, and 150 kJ/mol for octahedrons. This is due to the different reactivity of each CeO_2 crystalline plane emerging on the surface, which can affect the reaction mechanism. Xiao et al. [43] presented that the CO oxidation in the excess oxygen on porous and bulk $LaFeO_3$ is characterized by an observed activation energy of 78 and 31 kJ/mol, respectively, while porous $LaFeO_3$ had a lower t_{50}; the authors explained the increased activity of porous $LaFeO_3$ by its greater oxygen deficiency and electron enrichment due to the transition Fe^{3+}-O-Fe^{3+} → Fe^{4+}-($e^-\cdot\square$)-Fe^{3+} + 1/2O_2. Although the presence of Fe^{4+} was not analyzed for sample *G/N* = 0.8, its participation in the catalytic process cannot be ruled out. According to [53], the higher activity toward CO oxidation of $FeO_x/LaFeO_3$ is distinguished by a higher E_a^{obs} (90 kJ/mol) when compared to $LaFeO_3$ (79 kJ/mol). A comparison with literature data (Table 2) shows that the E_a^{obs} of the samples *G/N* = 0.2 and 1.4 are close to pure CeO_2; meanwhile, for sample *G/N* = 0.8, the E_a^{obs} approaches those of $LaMn_{0.8}B_{0.2}O_3$ (B=Ni, Zn, Cu) perovskites.

4. Conclusion

The RedOx conditions of the synthetic reaction mixture (glycine/nitrate ratios, *G/N*) were focused on to examine their effects on the phase, structural, specific surface area, reducibility, and catalytic properties of the obtained Ce–Fe–O-based nanopowders. It was discovered that various modes of reaction combustion result in differences in product characteristics due to differences in reaction zone temperatures, amounts and speeds of generated gases. As a result, depending on the *G/N* conditions, the synthesized catalysts possess two (c-CeO_2, am-F_2O_3), three (c-CeO_2, o-$CeFeO_3$, α-F_2O_3), or four phases (c-CeO_2, o-$CeFeO_3$, α-F_2O_3, am-Fe_2O_3). In general, as the *G/N* ratio increases, the average crystallite size decreases, causing the specific surface area to increase. Sample *G/N* = 1.2 (excess ratio of glycine) was found to be the optimal RedOx ratio for synthesizing the $CeO_2/CeFeO_3/Fe_2O_3$ nanocomposite with the highest catalytic activity when compared to the prepared samples. It was recommended to consider the catalyst's reducibility, observed activation energy, and reaction mechanism of H_2 oxidation in order to acquire a higher performance in hydrogen combustion. The resulting catalysis of such substances is paving the way for the development and design of low-cost catalysts regarding H_2 removal, which will contribute to preventing hydrogen-related accidents like explosions and fires.

Declaration of competing interest

The authors declare that they have no known competing financial interests or personal relationships that could have appeared to influence the work reported in this paper.

Acknowledgments

The authors are grateful to E.A. Zaboeva for her assistance in carrying out the synthesis of Ce–Fe–O-based nanopowders using the glycine-nitrate combustion method. This research did not receive any specific grant from funding agencies in the public, commercial, or not-for-profit sectors.

References

[1] V. Shepelin, D. Koshmanov, E. Chepelin, Catalysts for hydrogen removal: kinetic paradox and functioning at high concentration of hydrogen, Int. Conf. Hydrog. Saf. (2009) 1–12.
[2] C.J. Leppard, A. Holt, Process for the removal of hydrogen from Gases, 1983. EP 0 089 183 A2).
[3] Z. Du, C. Liu, J. Zhai, X. Guo, Y. Xiong, W. Su, G. He, A review of hydrogen purification technologies for fuel cell vehicles, Catalysts 11 (2021) 393, https://doi.org/10.3390/catal11030393.
[4] J. Depken, A. Dyck, L. Roß, S. Ehlers, Safety considerations of hydrogen application in shipping in comparison to LNG, Energies 15 (2022) 3250, https://doi.org/10.3390/en15093250.
[5] B.V. L'vov, A.K. Galwey, Catalytic oxidation of hydrogen on platinum, J. Therm. Anal. Calorim. 112 (2013) 815–822, https://doi.org/10.1007/s10973-012-2567-0.
[6] T.C. Golden, J.R. Hufton, M.A. Kalbassi, G.C. Lau, C. Waweru, C.J. Raiswell, C. Suggitt, D.P. Zwilling, Removal of hydrogen and Carbon monoxide impurities from Gas streams using a Copper and manganese based Catalyst, 2014. EP 2 789 376 A1.
[7] A.N. Matveyeva, S.O. Omarov, M.A. Gavrilova, D.A. Sladkovskiy, D.Y. Murzin, $CeFeO_3$-CeO_2-Fe_2O_3 systems: synthesis by solution combustion method and catalytic performance in CO_2 hydrogenation, Materials 15 (2022) 7970, https://doi.org/10.3390/ma15227970.
[8] T.S. Cam, S.O. Omarov, M.I. Chebanenko, S.G. Izotova, V.I. Popkov, Recent progress in the synthesis of CeO_2-based nanocatalysts towards efficient oxidation of CO, J. Sci. Adv. Mater. Devices. 7 (2022) 100399, https://doi.org/10.1016/j.jsamd.2021.11.001.
[9] T.S. Cam, S.O. Omarov, M.I. Chebanenko, A.S. Sklyarova, V.N. Nevedomskiy, V.I. Popkov, One step closer to the low-temperature CO oxidation over non-noble CuO/CeO_2 nanocatalyst: the effect of CuO loading, J. Environ. Chem. Eng. 9 (2021) 105373, https://doi.org/10.1016/j.jece.2021.105373.
[10] N. Tien Thao, L.T. Son, Production of cobalt-copper from partial reduction of $La(Co,Cu)O_3$ perovskites for CO hydrogenation, J. Sci. Adv. Mater. Devices. 1 (2016) 337–342, https://doi.org/10.1016/j.jsamd.2016.07.011.
[11] A. Pinheiro, A. Oliveira, F. de Sousa, J. Soares, G. Saraiva, A. Oliveira, R. Lang, CeFe-based bead nanocomposites as catalysts for oxidation of ethylbenzene reaction, Catalysts 8 (2018) 495, https://doi.org/10.3390/catal8110495.
[12] Z. Zeng, Y. Xu, Z. Zhang, Z. Gao, M. Luo, Z. Yin, C. Zhang, J. Xu, B. Huang, F. Luo, Y. Du, C. Yan, Rare-earth-containing perovskite nanomaterials: design, synthesis, properties and applications, Chem. Soc. Rev. 49 (2020) 1109–1143, https://doi.org/10.1039/C9CS00330D.
[13] E. Saputra, P.S. Utama, I. Hs, M.D.V. Simatupang, B.A. Prawiranegara, H.R. Abid, O. Muraza, Spent bleaching earth supported $CeFeO_3$ perovskite for visible light photocatalytic oxidation of methylene blue, J. Appl. Mater. Technol. 1 (2020) 81–87, https://doi.org/10.31258/Jamt.1.2.81-87.
[14] C.E. Choong, C.M. Park, Y.-Y. Chang, J. Yang, J.R. Kim, S.-E. Oh, B.-H. Jeon, E.H. Choi, Y. Yoon, M. Jang, Interfacial coupling perovskite $CeFeO_3$ on layered graphitic carbon nitride as a multifunctional Z-scheme photocatalyst for

boosting nitrogen fixation and organic pollutants demineralization, Chem. Eng. J. 427 (2022) 131406, https://doi.org/10.1016/j.cej.2021.131406.
[15] P. Tang, J. Zhang, M. Fu, F. Cao, C. Lv, Characterization and preparation nanosized $CeFeO_3$ by a microwave process, Integrated Ferroelectrics Int. J. 146 (2013) 99–104, https://doi.org/10.1080/10584587.2013.789756.
[16] D. Ni, Q. Yang, J. Li, J. Ying, C. Tang, P. Tang, Preparation of Ni-doped $CeFeO_3$ by microwave process and its visible-light photocatalytic activity, J. Nanosci. Nanotechnol. 16 (2016) 1046–1049, https://doi.org/10.1166/jnn.2016.10798.
[17] J. Ameta, A. Kumar, R. Ameta, V.K. Sharma, S.C. Ameta, Synthesis and characterization of $CeFeO_3$ photocatalyst used in photocatalytic bleaching of gentian violet, J. Iran. Chem. Soc. 6 (2009) 293–299, https://doi.org/10.1007/BF03245837.
[18] L. Hou, L. Shi, J. Zhao, S. Zhou, S. Pan, X. Yuan, Y. Xin, Room-temperature multiferroicity in $CeFeO_3$ ceramics, J. Alloys Compd. 797 (2019) 363–369, https://doi.org/10.1016/j.jallcom.2019.05.078.
[19] S.J. Yuan, Y.M. Cao, L. Li, T.F. Qi, S.X. Cao, J.C. Zhang, L.E. DeLong, G. Cao, First-order spin reorientation transition and specific-heat anomaly in $CeFeO_3$, J. Appl. Phys. 114 (2013) 113909, https://doi.org/10.1063/1.4821516.
[20] M. Robbins, G.K. Wertheim, A. Menth, R.C. Sherwood, Preparation and properties of polycrystalline cerium orthoferrite ($CeFeO_3$), J. Phys. Chem. Solid. 30 (1969) 1823–1825, https://doi.org/10.1016/0022-3697(69)90250-9.
[21] A. Varma, A.S. Mukasyan, A.S. Rogachev, K.V. Manukyan, Solution combustion synthesis of nanoscale materials, Chem. Rev. 116 (2016) 14493–14586, https://doi.org/10.1021/acs.chemrev.6b00279.
[22] L.L. Petschnig, G. Fuhrmann, D. Schildhammer, M. Tribus, H. Schottenberger, H. Huppertz, Solution combustion synthesis of $CeFeO_3$ under ambient atmosphere, Ceram. Int. 42 (2016) 4262–4267, https://doi.org/10.1016/j.ceramint.2015.11.102.
[23] V.V. Zvereva, V.I. Popkov, Synthesis of CeO_2-Fe_2O_3 nanocomposites via controllable oxidation of $CeFeO_3$ nanocrystals, Ceram. Int. 45 (2019) 12516–12520, https://doi.org/10.1016/j.ceramint.2019.03.188.
[24] E.A. Zaboeva, S.G. Izotova, V.I. Popkov, Glycine-nitrate combustion synthesis of $CeFeO_3$-based nanocrystalline powders, Russ. J. Appl. Chem. 89 (2016) 1228–1236, https://doi.org/10.1134/S1070427216080036.
[25] K.D. Martinson, I.S. Kondrashkova, V.I. Popkov, Synthesis of $EuFeO_3$ nanocrystals by glycine-nitrate combustion method, Russ. J. Appl. Chem. 90 (2017) 1214–1218, https://doi.org/10.1134/S1070427217080031.
[26] K.D. Martinson, I.S. Kondrashkova, M.I. Chebanenko, A.S. Kiselev, T.Y. Kiseleva, V.I. Popkov, Morphology, structure and magnetic behavior of orthorhombic and hexagonal $HoFeO_3$ synthesized via solution combustion approach, J. Rare Earths 40 (2022) 296–301, https://doi.org/10.1016/j.jre.2021.01.001.
[27] F. Tomul, Y. Arslan, B. Kabak, D. Trak, E. Kendüzler, E.C. Lima, H.N. Tran, Peanut shells-derived biochars prepared from different carbonization processes: comparison of characterization and mechanism of naproxen adsorption in water, Sci. Total Environ. 726 (2020) 137828, https://doi.org/10.1016/j.scitotenv.2020.137828.
[28] C.D. Scott, Kinetics of the Catalyzed oxidation of hydrogen, Carbon monoxide, and methane by oxygen in a flowing stream of helium, Oak Ridge Natl. Lab., 1961, https://doi.org/10.2172/4086810.
[29] J.P. Bonnelle, B. Delmon, E. Derouane, Surface Properties and Catalysis by Non-Metals, Springer Netherlands, Dordrecht, 1983, https://doi.org/10.1007/978-94-009-7160-8.
[30] S. Sourirajan, M.A. Accomazzo, Catalytic oxidation of carbon monoxide present in low concentrations, Can. J. Chem. 38 (1960) 1990–1998, https://doi.org/10.1139/v60-268.
[31] A.N. Matveyeva, J. Wärnå, N.A. Pakhomov, D. Yu. Murzin, Kinetic modeling of isobutane dehydrogenation over Ga_2O_3/Al_2O_3 catalyst, Chem. Eng. J. 381 (2020) 122741, https://doi.org/10.1016/j.cej.2019.122741.
[32] T.S. Cam, T.A. Vishnevskaya, S.O. Omarov, V.N. Nevedomskiy, V.I. Popkov, Urea-nitrate combustion synthesis of CuO/CeO_2 nanocatalysts toward low-temperature oxidation of CO: the effect of Red/Ox ratio, J. Mater. Sci. 55 (2020) 11891–11906, https://doi.org/10.1007/s10853-020-04857-3.
[33] M. Thommes, K. Kaneko, A.V. Neimark, J.P. Olivier, F. Rodriguez-Reinoso, J. Rouquerol, K.S.W. Sing, Physisorption of gases, with special reference to the evaluation of surface area and pore size distribution (IUPAC Technical Report), Pure Appl. Chem. 87 (2015) 1051–1069, https://doi.org/10.1515/pac-2014-1117.
[34] J. Li, Z. Wang, X. Yang, L. Hu, Y. Liu, C. Wang, Evaluate the pyrolysis pathway of glycine and glycylglycine by TG–FTIR, J. Anal. Appl. Pyrolysis 80 (2007) 247–253, https://doi.org/10.1016/j.jaap.2007.03.001.
[35] Z. Gu, K. Li, S. Qing, X. Zhu, Y. Wei, Y. Li, H. Wang, Enhanced reducibility and redox stability of Fe_2O_3 in the presence of CeO_2 nanoparticles, RSC Adv. 4 (2014) 47191–47199, https://doi.org/10.1039/C4RA06715K.
[36] K. Li, M. Haneda, Z. Gu, H. Wang, M. Ozawa, Modification of CeO_2 on the redox property of Fe2O3, Mater. Lett. 93 (2013) 129–132, https://doi.org/10.1016/j.matlet.2012.09.039.
[37] W. Zhang, X. Shi, M. Gao, J. Liu, Z. Lv, Y. Wang, Y. Huo, C. Cui, Y. Yu, H. He, Iron-based composite oxide catalysts tuned by CTAB exhibit superior NH3-SCR performance, Catalysts 11 (2021) 224, https://doi.org/10.3390/catal11020224.
[38] W. Ning, B. Li, B. Wang, X. Yang, Y. Jin, Enhanced production of C_{5+} hydrocarbons from CO_2 hydrogenation by the synergistic effects of Pd and K on γ-Fe_2O_3 catalyst, Catal. Lett. 149 (2019) 431–440, https://doi.org/10.1007/s10562-018-2622-y.
[39] O. Matz, M. Calatayud, Breaking H2 with CeO_2: effect of surface termination, ACS Omega 3 (2018) 16063–16073, https://doi.org/10.1021/acsomega.8b02410.
[40] S.O. Omarov, K.D. Martinson, A.N. Matveyeva, M.I. Chebanenko, V.N. Nevedomskiy, V.I. Popkov, Renewable hydrogen production via glycerol steam reforming over Ni/CeO_2 catalysts obtained by solution combustion method: the effect of Ni loading, Fuel Process. Technol. 236 (2022) 107429, https://doi.org/10.1016/j.fuproc.2022.107429.
[41] J. He, H. Zhang, W. Wang, P. Yao, Y. Jiao, J. Wang, Y. Chen, Soot combustion over CeO_2 catalyst: the influence of biodiesel impurities (Na, K, Ca, P) on surface chemical properties, Environ. Sci. Pollut. Res. 28 (2021) 26018–26029, https://doi.org/10.1007/s11356-020-11918-2.
[42] T. Désaunay, G. Bonura, V. Chiodo, S. Freni, J.-P. Couzinié, J. Bourgon, A. Ringuedé, F. Labat, C. Adamo, M. Cassir, Surface-dependent oxidation of H_2 on CeO_2 surfaces, J. Catal. 297 (2013) 193–201, https://doi.org/10.1016/j.jcat.2012.10.011.
[43] P. Xiao, L. Zhong, J. Zhu, J. Hong, J. Li, H. Li, Y. Zhu, CO and soot oxidation over macroporous perovskite $LaFeO_3$, Catal. Today 258 (2015) 660–667, https://doi.org/10.1016/j.cattod.2015.01.007.
[44] X. Liao, Y. Zhang, J. Guo, L. Zhao, M. Hill, Z. Jiang, Y. Zhao, The catalytic hydrogenation of maleic anhydride on $CeO_{2-\delta}$-supported transition metal catalysts, Catalysts 7 (2017) 272, https://doi.org/10.3390/catal7090272.
[45] D.R. Mullins, P.M. Albrecht, F. Calaza, Variations in reactivity on different crystallographic orientations of cerium oxide, Top. Catal. 56 (2013) 1345–1362, https://doi.org/10.1007/s11244-013-0146-7.
[46] M.J. Manto, P. Xie, C. Wang, Catalytic dephosphorylation using ceria nanocrystals, ACS Catal. 7 (2017) 1931–1938, https://doi.org/10.1021/acscatal.6b03472.
[47] M. Machida, T. Kawada, H. Fujii, S. Hinokuma, The role of CeO_2 as a gateway for oxygen storage over CeO_2-grafted Fe_2O_3 composite materials, J. Phys. Chem. C 119 (2015) 24932–24941, https://doi.org/10.1021/acs.jpcc.5b09876.
[48] B. Kucharczyk, K. Adamska, W. Tylus, W. Miśta, B. Szczygieł, J. Winiarski, Effect of silver addition to $LaFeO_3$ perovskite on the activity of monolithic $La_{1-x}Ag_xFeO_3$ perovskite catalysts in methane hexane oxidation, Catal. Lett. 149 (2019) 1919–1933, https://doi.org/10.1007/s10562-019-02779-7.
[49] V.M. Shinde, G. Madras, Kinetic studies of ionic substituted copper catalysts for catalytic hydrogen combustion, Catal. Today 198 (2012) 270–279, https://doi.org/10.1016/j.cattod.2012.02.019.
[50] V.M. Shinde, G. Madras, Nanostructured Pd modified Ni/CeO_2 catalyst for water gas shift and catalytic hydrogen combustion reaction, Appl. Catal. B Environ. 132–133 (2013) 28–38, https://doi.org/10.1016/j.apcatb.2012.11.021.
[51] X. Liu, J. Liu, Z. Chang, X. Sun, Y. Li, Crystal plane effect of Fe_2O_3 with various morphologies on CO catalytic oxidation, Catal. Commun. 12 (2011) 530–534, https://doi.org/10.1016/j.catcom.2010.11.016.
[52] H. Bao, X. Chen, J. Fang, Z. Jiang, W. Huang, Structure-activity relation of Fe_2O_3-CeO_2 composite catalysts in CO oxidation, Catal. Lett. 125 (2008) 160–167, https://doi.org/10.1007/s10562-008-9540-3.
[53] Q. Yang, J. Li, D. Wang, Y. Peng, Y. Ma, Activity improvement of acid treatment on $LaFeO_3$ catalyst for CO oxidation, Catal. Today 376 (2021) 205–210, https://doi.org/10.1016/j.cattod.2020.05.056.
[54] F.-C. Buciuman, F. Patcas, J.-C. Menezo, J. Barbier, T. Hahn, H.-G. Lintz, Catalytic properties of $La_{0.8}A_{0.2}MnO_3$ (A = Sr, Ba, K, Cs) and $LaMn_{0.8}B_{0.2}O_3$ (B = Ni, Zn, Cu) perovskites: 1. Oxidation of hydrogen and propene, Appl. Catal. B Environ. 35 (2002) 175–183, https://doi.org/10.1016/S0926-3373(01)00250-8.